# CANDIDATES FOR ASTEROID DUST TRAILS

DAVID NESVORNÝ,[1] MARK SYKES,[2] DAVID J. LIEN,[2] JOHN STANSBERRY,[3] WILLIAM T. REACH,[4] DAVID VOKROUHLICKÝ,[1]
WILLIAM F. BOTTKE,[1] DANIEL D. DURDA,[1] SUMITA JAYARAMAN,[2] AND RUSSELL G. WALKER[5]

## ABSTRACT

The contribution of different sources to the circumsolar dust cloud (known as the zodiacal cloud) can be deduced from diagnostic observations. We used the *Spitzer Space Telescope* to observe the diffuse thermal emission of the zodiacal cloud near the ecliptic. Several structures were identified in these observations, including previously known asteroid dust bands, which are thought to have been produced by recent asteroid collisions, and cometary trails. Interestingly, two of the detected dust trails, denoted t1 and t2 here, cannot be linked to any known comet. Trails t1 and t2 represent a much larger integrated brightness than all known cometary trails combined and may therefore be major contributors to the circumsolar dust cloud. We used our *Spitzer* observations to determine the orbits of these trails and were able to link them to two ("orphan" or type II) trails that were discovered by the *Infrared Astronomical Satellite* (*IRAS*) in 1983. The orbits of trails t1 and t2 that we determined by combining the *Spitzer* and *IRAS* data have semi-major axes, eccentricities, and inclinations like those of the main-belt asteroids. We therefore propose that trails t1 and t2 were produced by very recent (≲100 kyr old) collisional breakups of small, ≲10 km diameter main-belt asteroids.

*Key words:* comets: general — interplanetary medium — minor planets, asteroids

## 1. INTRODUCTION

The circumsolar dust cloud (known as the zodiacal cloud [ZC]) is an excellent laboratory for the study of debris disks and their interaction with planets. Over the past two decades, NASA's space-borne facilities, such as the *Infrared Astronomical Satellite* (*IRAS*), the *Cosmic Background Explorer*, and the *Long-Duration Exposure Facility*, have probed the spatial distribution of the ZC, accretion rates of dust particles on the Earth, the origin of interplanetary dust particles, etc. The analysis of data from these instruments provides a baseline for interpreting features of the debris disks that were discovered around many stars (e.g., see Greaves et al. [2004, 2005] for recent examples).

It is believed that cometary activity and asteroid collisions are the two major contributors to the ZC. The proportions in which these two sources contribute to the ZC, however, have yet to be precisely determined. Observed cometary trails and asteroid dust bands provide important constraints on this problem.

Cometary dust trails were first observed by *IRAS* (Sykes 1986) and consist of large refractory particles ejected from Jupiter-family comets (JFCs) at low speeds. Consequently, they tend to be found near the orbital paths of their parent bodies. The infrared (IR) brightness and length of a trail can be used to determine the comet mass loss (Sykes & Walker 1992). For example, the total mass lost from comet 2P/Encke during its 1997 apparition is estimated to be $(2-6) \times 10^{13}$ g (Reach et al. 2000).

Asteroid dust bands were also discovered by *IRAS* as extended sources of IR emission roughly parallel to the ecliptic (Low et al. 1984). These structures were produced by disruptive collisions of large, ≳10 km diameter main-belt asteroids (Dermott et al. 1984; Sykes & Greenberg 1986). Precise modeling of these observations has been used to determine the contribution of disrupted large asteroids to the ZC (e.g., Grogan et al. 2001 and references therein).

The results indicate that the two prominent *IRAS* dust bands at inclinations[6] ≈2°.1 and ≈9°.3 are by-products of two recent asteroid disruption events. The former is associated with a disruption of an ≈30 km diameter asteroid occurring 5.8 Myr ago; this event gave birth to the Karin cluster (Nesvorný et al. 2002). The latter came from a breakup of a large, >100 km diameter asteroid ≈8.3 Myr ago that produced the Veritas family (Nesvorný et al. 2003). Together, particles from the Karin and Veritas families contribute by ≈5% of the ZC brightness in the wavelength range 10–60 $\mu$m and for $-50° < b < 50°$, where $b$ is the ecliptic latitude (Nesvorný et al. 2006b).

Using the *Spitzer Space Telescope*, we observed the diffuse thermal emission of the ZC near the ecliptic and found candidates for the *asteroid dust trails*, which may have been produced by much more recent (≲100 kyr old) asteroid collisions than those that produced the asteroid dust bands. If indeed asteroidal by origin, these trails may help us to determine the collective contribution of disrupted small asteroids to the ZC. This contribution is likely to be important because the two identified trails represent a much larger integrated brightness than all known cometary trails combined.

Here we describe our new *Spitzer* observations of trails (§ 2), show how source orbits of observed trails can be determined (§ 3), link them to *IRAS* observations (§ 4), and determine the orbits by combining the *Spitzer* and *IRAS* data sets (§ 5). Implications of this work are discussed in § 6.

## 2. OBSERVATIONS

We used the 24 $\mu$m MIPS array of *Spitzer* to obtain four sets (A, B, C, D) of four parallel scans (1, 2, 3, 4). The scans are 5'.4 wide and go from $+10°$ down to $-10°$ in ecliptic latitude, $b$,

---

[1] Department of Space Studies, Southwest Research Institute, 1050 Walnut Street, Suite 400, Boulder, CO 80302.

[2] Planetary Science Institute, 1700 East Fort Lowell, Suite 106, Tucson, AZ 85719.

[3] Steward Observatory, University of Arizona, 933 North Cherry Avenue, Tucson, AZ 85721-0065.

[4] California Institute of Technology, *Spitzer* Science Center, 1200 East California Boulevard, Pasadena, CA 91125.

[5] Monterey Institute for Research in Astronomy, 200 Eighth Street, Marina, CA 93933.

[6] Inclinations are defined here with respect to the invariant plane of the planets.

TABLE 1
Basic Information for Our 16 Noodles

| ID (1) | Day (mm/dd/yy) (2) | Scan Dir. (3) | No. Pixels (4) | $t$ (JD − 2,453,300) (5) | $l_{Spitzer}$ (deg) (6) | $b_{Spitzer}$ (deg) (7) | $R_{Spitzer–Sun}$ (AU) (8) | Obs. $l$ (deg) (9) | Elong. (deg) (10) | 24 $\mu$m (MJy sr$^{-1}$) (11) |
|---|---|---|---|---|---|---|---|---|---|---|
| A1............ | 12/01/04 | Trail | 29123 | 41.00739 | 61.7377 | 1.0954 | 1.012608 | 354.0061 | 112.26 | 46.52 |
| A2............ | 12/03/04 | Trail | 28974 | 42.60715 | 63.2857 | 1.0868 | 1.012305 | 355.5061 | 112.22 | 46.59 |
| A3............ | 12/04/04 | Trail | 28974 | 44.08755 | 64.7190 | 1.0783 | 1.012024 | 357.0061 | 112.28 | 46.63 |
| A4............ | 12/06/04 | Trail | 28974 | 45.62665 | 66.2101 | 1.0686 | 1.011733 | 358.5061 | 112.29 | 46.60 |
| B1............ | 12/27/04 | Trail | 28974 | 66.73215 | 86.7415 | 0.8658 | 1.007876 | 354.0061 | 87.26 | 66.22 |
| B2............ | 12/28/04 | Trail | 28974 | 68.16565 | 88.1413 | 0.8477 | 1.007630 | 355.5061 | 87.26 | 66.19 |
| B3............ | 12/30/04 | Trail | 28974 | 69.69305 | 89.6340 | 0.8277 | 1.007372 | 357.0061 | 87.37 | 66.14 |
| B4............ | 12/31/04 | Trail | 28974 | 71.33755 | 91.2417 | 0.8055 | 1.007098 | 358.5061 | 87.26 | 66.31 |
| C1............ | 12/27/04 | Lead | 34047 | 67.23748 | 87.2348 | 0.8595 | 1.007789 | 178.9928 | 88.24 | 61.87 |
| C2............ | 12/29/04 | Lead | 28974 | 68.84678 | 88.8069 | 0.8388 | 1.007515 | 180.4928 | 88.31 | 61.85 |
| C3............ | 12/30/04 | Lead | 28974 | 70.42108 | 90.3456 | 0.8179 | 1.007250 | 181.9928 | 88.35 | 61.77 |
| C4............ | 01/01/05 | Lead | 28974 | 71.99917 | 91.8887 | 0.7964 | 1.006989 | 183.4928 | 88.39 | 61.80 |
| D1............ | 01/24/05 | Lead | 32356 | 94.84678 | 114.3112 | 0.4272 | 1.003759 | 178.9928 | 115.31 | 44.27 |
| D2............ | 01/25/05 | Lead | 28974 | 96.19448 | 115.6379 | 0.4027 | 1.003606 | 180.4928 | 115.14 | 44.40 |
| D3............ | 01/27/05 | Lead | 28974 | 97.62028 | 117.0420 | 0.3766 | 1.003451 | 181.9928 | 115.04 | 44.46 |
| D4............ | 01/28/05 | Lead | 28974 | 99.32338 | 118.7197 | 0.3451 | 1.003272 | 183.4928 | 115.22 | 44.34 |

Notes.—The columns are: (1) noodle identification; (2) observation date; (3) scanning direction; (4) total number of pixels obtained; (5) exact time when each scan crossed the ecliptic; (6)–(8) ecliptic longitude and latitude of *Spitzer*'s position and its distance from the Sun at the time shown in col. (5); (9) and (10) *Spitzer*-centric ecliptic longitude and solar elongation of the observing direction; and (11) measured 24 $\mu$m flux at the ecliptic.

except for scans C1 and D1, which reach down to $b = -13°.5$ and $-14°.4$, respectively. Individual scans in each set run roughly parallel to each other across the ecliptic and are separated by $1°.5$ in ecliptic longitude, $l$.

By co-adding all 128 pixels cross-scan, the MIPS images were used to generate "noodles" (M. V. Sykes et al. 2006, in preparation) with $2''.5$ in scan resolution that show profiles of the diffuse IR flux in 24 $\mu$m as a function of $b$. These profiles provide much better sensitivity (about 10 times) and spatial resolution ($2''.5$; about 20 times) than *IRAS* observations. Table 1 lists general information for our 16 noodles. Figure 1 shows the observed IR fluxes.

As expected, the observed emission peaks near the ecliptic. It shows broad shoulders, several degrees apart in ecliptic latitude, corresponding to the inner dust bands (denoted $\alpha$ and $\beta$ in Sykes 1986). Sets B and C show stronger signals than sets A and D because of differences in solar elongation. In sets B and C, where the elongation is smaller, the shoulders are narrower because the source of the emission is seen from a larger distance. Several additional humps in the flux profiles are also apparent (e.g., for $b \approx -7°$ and $b \approx 5°.5$ in set D).

We used a Fourier filter to enhance small-scale structures in the noodles (see Reach et al. [1997] and Nesvorný et al. [2006b] for a description of the filter). The filter suppressed structures in the signal with latitudinal spreads $<0°.1$ and $>4°$. Figure 2 shows the filtered profiles. Structures corresponding to the asteroid dust bands and trails clearly appear and are denoted in the figure.

The inner dust bands $\alpha$ and $\beta$ (Sykes 1986) are nicely resolved, especially in set D. The $\beta$-band pair appears to be $\approx 50\%$ brighter than the $\alpha$-band pair. The southern component of the $\gamma$ band shows $b \approx -9°$ in noodle C1 (Fig. 2c, *bottom line*) as a pyramidal peak rising about 0.2 MJy sr$^{-1}$ above the background. Noodle C1 had a favorable geometry and was extended past $-10°$, which allowed us to determine the filtered signal down to $b \approx -10°$. In other, shorter legs of set C, the southern component of the $\gamma$ band produces an increasing flux intensity downward to $b \approx -9°$. The same feature can be seen at positive latitudes in set B.

Three major trails are denoted in Figure 2:

1. Trail 1, denoted t1, can be seen at $b \approx 4°.3$ in set C and $b \approx 5°.5$ in set D. It shows up as peaks that are $\approx 1°$ wide and 0.2 MJy sr$^{-1}$ high. These peaks in two different sets of scans correspond to the same trail because the observing longitude for sets C and D was similar (Table 1). In set D the hump corresponding to this trail is clearly split, showing two (or perhaps even three) peaks separated by about $0°.3–0°.4$ in latitude (Fig. 3). We denote these peaks t1a (the one at larger $b$) and t1b (the one at smaller $b$); t1b appears as a shoulder of t1 in set C.

2. Trail 2, denoted t2, appears at $b \approx -6°$ in set C and at $b \approx -7°.5$ in set D as humps in the signal approximately $1°$ wide and 0.1–0.2 MJy sr$^{-1}$ high. The humps have a broad and concave structure (Fig. 3).

3. Trail 3, denoted t3, is a sharp peak at $b \approx 7°.5–8°$ in all scans of sets A and B. With increasing longitude (following scan sequence 1, 2, 3, 4 in both sets), the exact location of the peak shifts to larger latitudes.

It is important to determine the sources of these trails because these sources apparently supply large quantities of dust to the ZC. For example, the peak surface brightness of t2 in our *Spitzer* data is 0.22 MJy sr$^{-1}$, and its FWHM is $0°.72$. Therefore, the integrated flux is $\approx 0°.18$ MJy sr$^{-1}$ or about 910 MJy arcmin$^{-1}$. For a comparison, typical comet trails have one-dimensional integrated fluxes of 2–20 MJy arcmin$^{-1}$. Therefore, trail t2 is about 2 orders of magnitude stronger in one-dimensional flux than a bright comet trail. The integrated flux of trail t1 is similar to that of trail t2. Together, trails t1 and t2 probably represent a much larger surface area than all observed cometary trails combined.

To identify the source of these trails we first tried to link them with known comets. We used a large number of JFCs and long-periodic comets with present perihelion distance $q < 5.5$ AU (i.e., inside Jupiter's orbit) from Y. Fernández's list.[7] The orbit of each comet at the epoch of our *Spitzer* observations was obtained
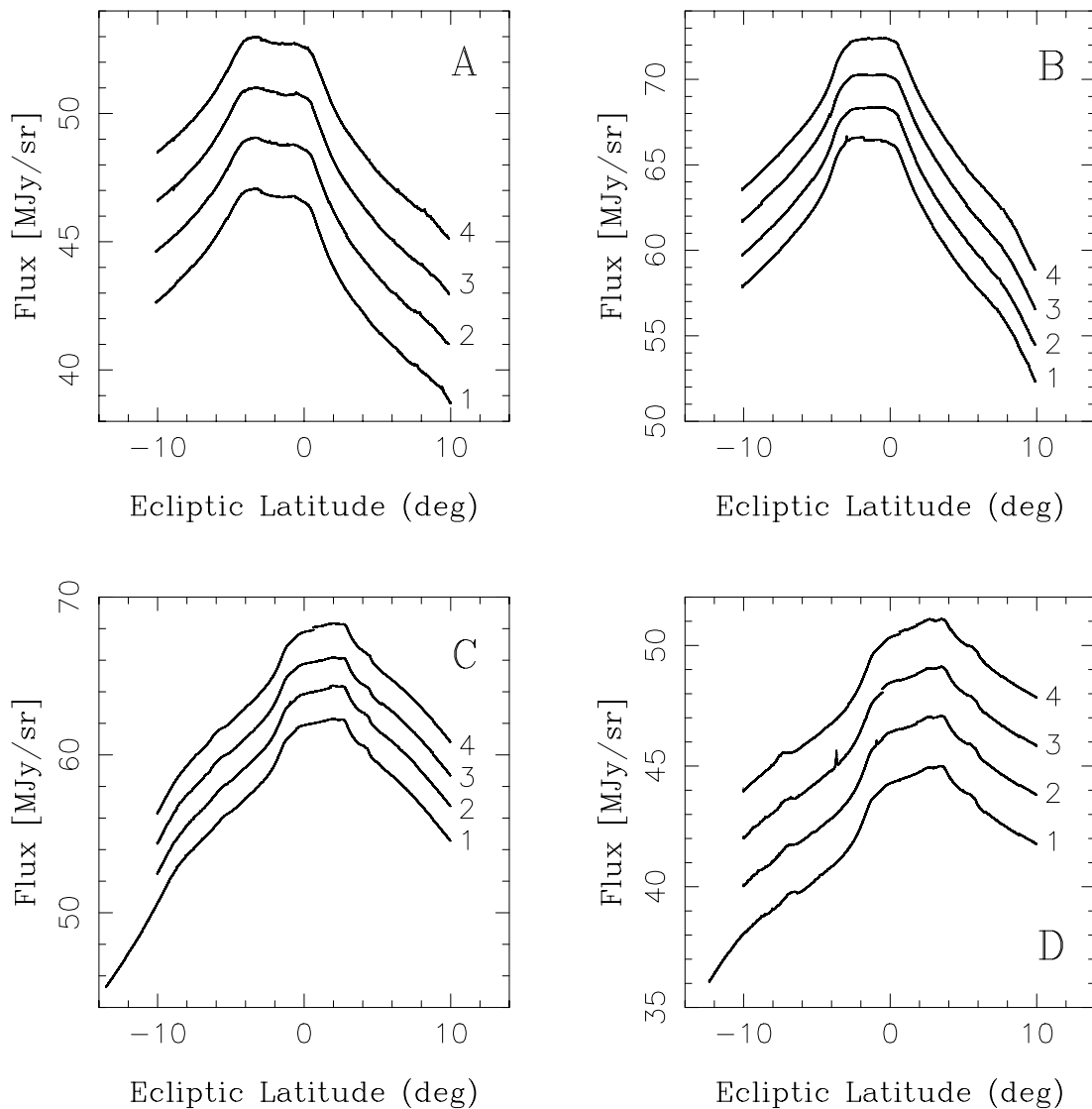
_____

[7] See http://www.physics.ucf.edu/~yfernandez/cometlist.html.

Fig. 1.—The 24 $\mu$m fluxes for our four sets (A, B, C, D) of four scans (1, 2, 3, 4). Scans 2, 3, and 4 in each set were offset by 2, 4, and 6 MJy sr$^{-1}$, respectively, relative to scan 1 to appear clearly in the plots. Individual segments in each scan, each about 1° in length, were joined smoothly by multiplying observed fluxes in each segment by a factor $f$, where $0.9 < f < 1.1$. This procedure removes from the signal the discontinuities between individual segments produced by the observation delays up to 6 hr. The value of the flux shown here can differ from the observed flux by up to 10%.

from the JPL's Horizons Web site.[8] We then determined the latitudes of orbits at longitudes corresponding to the individual scans. Finally, we compared those latitude values with the observed $b$ of trails t1, t2, and t3.

Based on this method we determined that the source of trail t3 is comet 29P/Schwassmann-Wachmann 1. A short trail behind 29P/Schwassmann-Wachmann 1 (about 10° long) was found by Sykes & Walker (1992) in the *IRAS* data and was studied by Stansberry et al. (2004) using *Spitzer*. This object has irregular outbursts due to sublimation of carbon dioxide ice. By chance, our *Spitzer* scans intersect this short trail between 3°.85 and 8°.75 in mean anomaly behind the location of 29P/Schwassmann-Wachmann 1, producing t3.

Interestingly, none of the known comets provided a satisfactory match to trails t1 and t2. Similarly, none of the meteoroid streams listed in Jopek et al. (2002) matches the location of t1 or

t2 in our *Spitzer* observations. Therefore, the origin of trails t1 and t2 has to be established by a different method.

### 3. ORBITAL FITS

One way to identify the source location of a trail is to determine its heliocentric orbit and compare it with the orbits of various populations of bodies in the solar system. For example, the main-belt asteroids have small eccentricities and inclinations and semimajor axes between 2 and 3.3 AU. The comets, on the other hand, tend to have large eccentricities and Jupiter-crossing orbits. Therefore, once the orbit of the trail is determined with a reasonable precision, it should be relatively easy to tell whether its source is asteroidal or cometary.

We used our *Spitzer* observations to solve for the orbits of trails t1, t2, and t3. We include trail t3 in this work, despite the fact that its orbit is known (it is that of comet 29P/Schwassmann-Wachmann 1), as a test case for our method. In the first step, we selected eight values of ecliptic latitude and longitude that best

---

[8] See http://ssd.jpl.nasa.gov/?horizons.
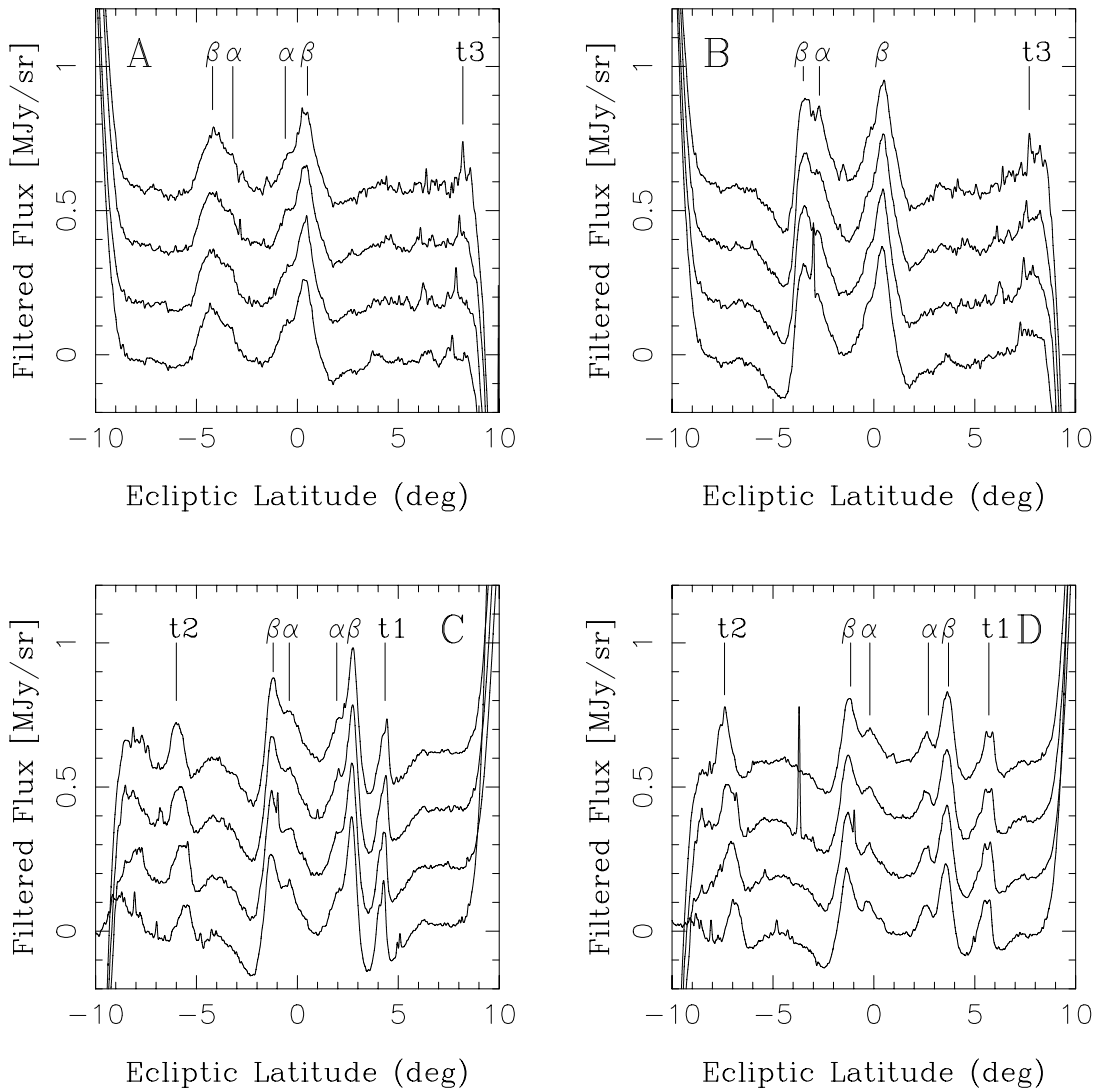
Fig. 2.—Filtered profiles. The original profiles shown in Fig. 1 were filtered to remove spatial features in ecliptic latitude $<0°.1$ and $>4°$. Inner asteroid dust bands ($\alpha$ and $\beta$; Sykes 1986) and trails (t1, t2, and t3) are denoted. The artifacts at extreme latitudes were produced by the filter.

correspond to t1, t2, and t3 in our *Spitzer* scans (each of these trails is seen in eight scans). The noodles were filtered to remove spatial features $>4°$. The high-frequency component was left in the signal. We fitted a polynomial to this filtered signal near the location of t1, t2, and t3 and determined the 1 $\sigma$ error of the measurements. The mean derived value is 0.009 MJy sr$^{-1}$, a value expected from the sensitivity of the *Spitzer* instrument (recall that 128 pixels were co-added cross-scan).

Next, we selected an approximate value for the observed $b$ of each peak. Using an interval of length $\Delta$ around this value, we fitted a second-order polynomial, $a_0 + a_1 b + a_2 b^2$, to the signal and determined the latitude of the maximum, $b_{\max} = -a_1/2a_2$. The uncertainties in $a_0$, $a_1$, and $a_2$ were used to determine 1 $\sigma$ errors of $b_{\max}$. This estimation of error is valid only if the parabolic profile can be satisfactorily fitted by a parabola, like in cases in which $\Delta$ is small. For large $\Delta$, we assumed that the error of $b_{\max}$ is 1′.

We used $\Delta = 0°.01$ and $0°.1$ for t1a, $\Delta \approx 0°.7$ for t1, $\Delta = 1°$ for t2, and $\Delta = 0°.01$ and $0°.1$ for t3. For small $\Delta$, $b_{\max}$ falls close to latitudes corresponding to the maximum of peaks shown in Figure 3. Fits with the $\Delta$ values that are more comparable to the latitudinal widths of peaks produce somewhat smaller $|b_{\max}|$ due to a slightly asymmetrical shape of the peaks (Fig. 3). Tables 2, 3, and 4 show the position of *Spitzer* and its pointing geometry at the

exact moment when it scanned over $b_{\max}$ corresponding to t1, t2, and t3, respectively.

In the second step, we sampled over $10^9$ heliocentric orbits for each trail with each orbit being defined by its semimajor axis, $a$, eccentricity, $e$, inclination, $i$, perihelion argument, $\omega$, and nodal longitude, $\Omega$. The orbits were then projected[9] onto the sky as they would be observed by *Spitzer* on the specific observation dates listed in Table 1. The *Spitzer*-centric latitude of an orbit, $b_{\mathrm{orb}}$, was determined at the intersection of each orbit with the *Spitzer* scans. We defined

$$\chi^2 = \sum_{j=1}^{N} \frac{\left(b_{\mathrm{orb}}^{(j)} - b_{\max}^{(j)}\right)^2}{\sigma_j^2}, \qquad (1)$$

where index $j$ denotes individual scans, $N = 8$, and $\sigma_j$ is the 1 $\sigma$ error of $b_{\max}^{(j)}$. Table 5 lists the orbital fits that produced the smallest $\chi^2$.

---

[9] The orbits and orbital elements used here, as well as the coordinates of the spacecraft, are heliocentric. Observing latitudes and longitudes are spacecraft-centric. We make rigorous transformations between these two reference systems in the fitting code.
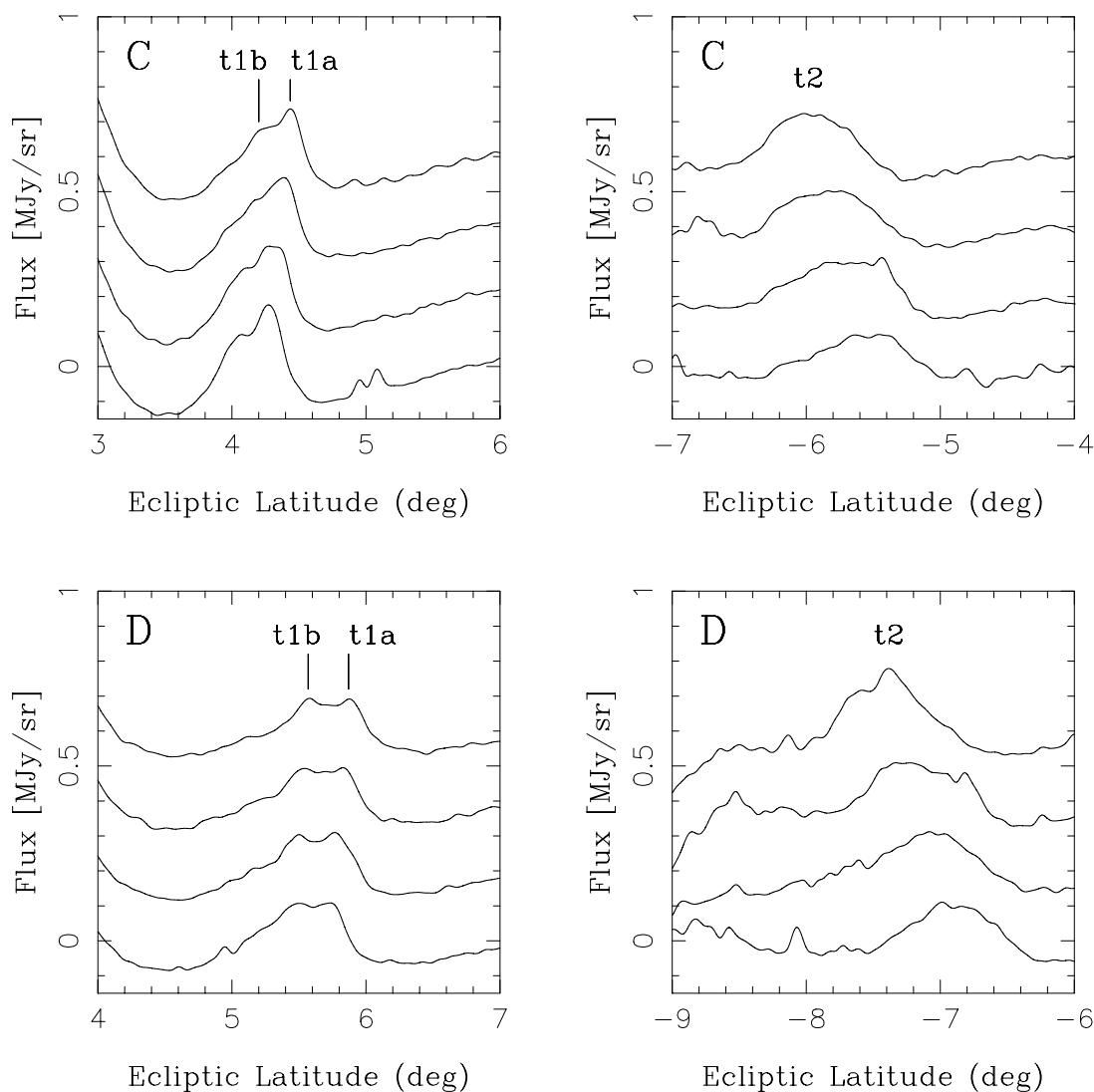
Fig. 3.—Part of the filtered profiles near trails t1 (*left*) and t2 (*right*). Trail t1 is split into two peaks, which we denote t1a and t1b. Trail t2 shows a complicated structure that changes with observing longitude *l*.

Figure 4 shows the best-fit orbits for t1a. The best-fit value of $\chi^2$ is 30.1 in this case ($\Delta = 0°1$; Table 5), which is larger than the number of observations used to determine the orbit ($N = 8$). Apparently, the maxima of the brightness cannot be fitted by an orbit with formal precision $\sigma_j$ determined by the polynomial fit.

This is an expected result, because the maxima of broad peaks in the filtered scans (Fig. 3) do not necessarily correspond to a single heliocentric orbit. Instead, the peaks are produced by a collection of particles moving in various, slightly different heliocentric orbits.

TABLE 2
*Spitzer* Data Used to Determine the Orbit for t1

| ID (1) | $t$ (JD) (2) | $l_{Spitzer}$ (deg) (3) | $b_{Spitzer}$ (deg) (4) | $R_{Spitzer}$ (AU) (5) | $l$ (deg) (6) | $b_{max}$ (deg) (7) | $\sigma$ (deg) (8) |
|---|---|---|---|---|---|---|---|
| C1.................. | 2,453,367.15235 | 87.15172 | 0.86064 | 1.0078036 | 178.99037 | 4.17780 | 0.0167 |
| C2.................. | 2,453,368.56178 | 88.52848 | 0.84259 | 1.0075637 | 180.49064 | 4.22084 | 0.0167 |
| C3.................. | 2,453,370.33052 | 90.25708 | 0.81920 | 1.0072656 | 181.99115 | 4.26353 | 0.0167 |
| C4.................. | 2,453,371.68517 | 91.58171 | 0.80074 | 1.0070410 | 183.49137 | 4.31087 | 0.0167 |
| D1.................. | 2,453,394.67231 | 114.13950 | 0.43038 | 1.0037796 | 179.00868 | 5.53633 | 0.0167 |
| D2.................. | 2,453,396.07735 | 115.52257 | 0.40493 | 1.0036190 | 180.50499 | 5.60700 | 0.0167 |
| D3.................. | 2,453,397.49888 | 116.92249 | 0.37892 | 1.0034641 | 182.00393 | 5.62779 | 0.0167 |
| D4.................. | 2,453,398.97856 | 118.38008 | 0.35149 | 1.0033082 | 183.50184 | 5.66783 | 0.0167 |

Notes.—We used $\Delta = 0°6$ for scans in set C and $\Delta = 0°8$ for scans in set D. The columns are: (1) scan identification label; (2) time of the observation; (3)–(5) ecliptic longitude, latitude, and heliocentric distance of *Spitzer* at the time shown in col. (2); (6) and (7) *Spitzer*-centric ecliptic longitude and latitude of t1 in each scan; and (8) error in $b_{max}$ (assumed to be 1′ here).

## TABLE 3
### *Spitzer* Data Used to Determine the Orbit for t2

| ID (1) | $t$ (JD) (2) | $l_{Spitzer}$ (deg) (3) | $b_{Spitzer}$ (deg) (4) | $R_{Spitzer}$ (AU) (5) | $l$ (deg) (6) | $b_{max}$ (deg) (7) | $\sigma$ (deg) (8) |
|---|---|---|---|---|---|---|---|
| C1.................. | 2,453,367.43201 | 87.42488 | 0.85707 | 1.0077559 | 178.99266 | −5.56792 | 0.0167 |
| C2.................. | 2,453,368.96677 | 88.92423 | 0.83728 | 1.0074953 | 180.49269 | −5.76779 | 0.0167 |
| C3.................. | 2,453,370.55071 | 90.47238 | 0.81621 | 1.0072290 | 181.99276 | −5.87124 | 0.0167 |
| C4.................. | 2,453,372.13063 | 92.01731 | 0.79467 | 1.0069677 | 183.49288 | −5.97346 | 0.0167 |
| D1.................. | 2,453,394.98972 | 114.45187 | 0.42465 | 1.0037424 | 178.96788 | −6.90220 | 0.0167 |
| D2.................. | 2,453,396.40732 | 115.84752 | 0.39889 | 1.0035833 | 180.45721 | −7.10439 | 0.0167 |
| D3.................. | 2,453,397.94762 | 117.36451 | 0.37062 | 1.0034168 | 181.95375 | −7.17214 | 0.0167 |
| D4.................. | 2,453,399.47546 | 118.86962 | 0.34225 | 1.0032566 | 183.44105 | −7.42063 | 0.0167 |

Notes.—We used $\Delta = 1°.0$. The columns are: (1) scan identification label; (2) time of the observation; (3)–(5) ecliptic longitude, latitude, and heliocentric distance of *Spitzer* at the time shown in col. (2); (6) and (7) *Spitzer*-centric ecliptic longitude and latitude of t1 in each scan; and (8) error in $b_{max}$ (assumed to be 1′ here).

## TABLE 4
### *Spitzer* Data Used to Determine the Orbit for t3

| ID (1) | $t$ (JD) (2) | $l_{Spitzer}$ (deg) (3) | $b_{Spitzer}$ (deg) (4) | $R_{Spitzer}$ (AU) (5) | $l$ (deg) (6) | $b_{max}$ (deg) (7) | $\sigma$ (deg) (8) |
|---|---|---|---|---|---|---|---|
| A1.................. | 2,453,340.84435 | 61.58003 | 1.09617 | 1.0126403 | 353.99221 | 7.66449 | 0.00306 |
| A2.................. | 2,453,342.44449 | 63.12826 | 1.08781 | 1.0123364 | 355.49765 | 7.86204 | 0.00125 |
| A3.................. | 2,453,343.92203 | 64.55884 | 1.07926 | 1.0120559 | 357.00216 | 8.02802 | 0.0008 |
| A4.................. | 2,453,345.45022 | 66.03915 | 1.06982 | 1.0117664 | 358.50686 | 8.19678 | 0.00098 |
| B1.................. | 2,453,366.57897 | 86.59191 | 0.86780 | 1.0079023 | 353.99743 | 7.25855 | 0.00116 |
| B2.................. | 2,453,367.95107 | 87.93190 | 0.85042 | 1.0076676 | 355.49224 | 7.42088 | 0.00163 |
| B3.................. | 2,453,369.52790 | 89.47257 | 0.82993 | 1.0074001 | 357.02609 | 7.56429 | 0.00136 |
| B4.................. | 2,453,371.11522 | 91.02425 | 0.80861 | 1.0071350 | 358.52117 | 7.70882 | 0.00123 |

Notes.—We used $\Delta = 0°.1$. Listed values of $\sigma_j$ were determined by the method described in the main text. The columns are: (1) scan identification label; (2) time of the observation; (3)–(5) ecliptic longitude, latitude, and heliocentric distance of *Spitzer* at the time shown in col. (2); (6) and (7) *Spitzer*-centric ecliptic longitude and latitude of t1 in each scan; and (8) error in $b_{max}$.

## TABLE 5
### Orbital Fits

| Parameter | Trail ID | | | | | | | | |
|---|---|---|---|---|---|---|---|---|---|
| | t1a | t1 | A | t1/A | t1/A | t2 | B | t2/B | t3 |
| Data[a]........................ | *Spitzer* | *Spitzer* | *IRAS* | *Spitzer/IRAS* | *Spitzer/IRAS* | *Spitzer* | *IRAS* | *Spitzer/IRAS* | *Spitzer* |
| $N$[b]............................. | 8 | 8 | 6 | 14 | 12 | 8 | 6 | 14 | 8 |
| $\Delta$[c] (deg) .................. | 0.1 | 0.6–0.8 | 0.7 | 0.7 | 0.7 | 1.0 | 0.7 | 1/0.7 | 0.1 |
| $\langle\sigma\rangle$[d] (arcmin)........... | 0.26 | 1.0 | 7.1 | 3.6 | 3.6 | 1.0 | 5.9 | 3.1 | 0.086 |
| $\chi^2$[e] ............................. | 30.1 | 1.9 | 8.0 | 80.0 | 15.0 | 26.8 | 87 | 830 | 159 |
| $\langle\delta b\rangle$[f] (arcmin)........... | 0.5 | 0.4 | 6.7 | 5.8 | 3.5 | 1.6 | 14 | 12 | 0.4 |
| $i$[g] (deg)..................... | 4.6 | 4.45 | 4.5 | 4.25 | 4.35 | 7.5 | 10 | 9 | 9.4 |
| $\delta i$[g] (deg).................. | 0.08 | 0.05 | 0.3 | 0.1 | 0.15 | 0.5 | 4 | 2 | 0.2 |
| $\Omega$[h] (deg) ................. | 85 | 83 | 65 | 64 | 76 | 294 | 300 | 300 | 313 |
| $\delta\Omega$[h] (deg)................. | 2 | 2 | 5 | 3 | 10 | 4 | 10 | 10 | 2 |
| $a_{circ}$[i] ........................ | 2.25 | 2.3 | 3.0 | 2–3 | 2–3 | 2.45 | ... | 2.45 | 5.85 |
| $e$[j] ............................. | <0.6 | <0.6 | <0.3 | 0.15–0.3 | <0.4 | <0.6 | Any | <0.35 | <0.3 |

[a] Data set used to determine the orbits.
[b] Number of selected observations.
[c] $\Delta$ (see main text for definition).
[d] Mean value of the error of $b_{max}$ (assumed to be 1′ for $\Delta > 0°.5$; determined by the method described in the main text for $\Delta < 0°.5$).
[e] $\chi^2$ of the best fit (eq. [1]).
[f] Mean standard deviation of $b_{orb}$ from $b_{max}$.
[g] Inclination and its 95.4% confidence range.
[h] Nodal longitude and its 95.4% confidence range.
[i] Semimajor axis of a near-circular orbit that fits data within the 95.4% confidence level or the range of the semimajor axis values in the fifth and sixth columns.
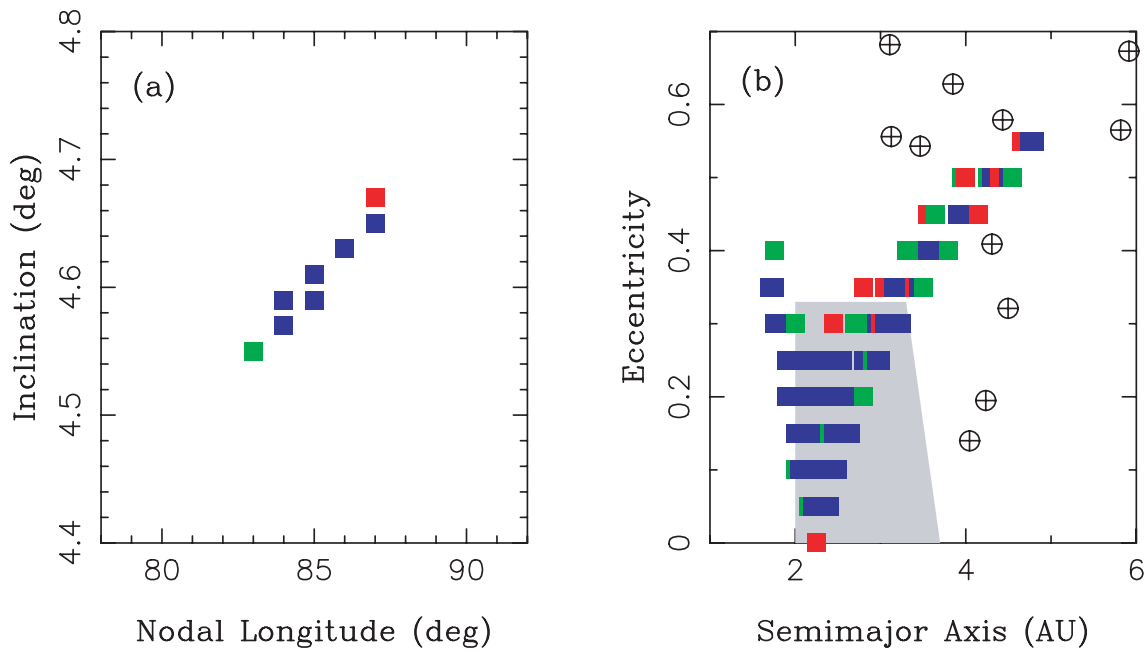[j] Range of eccentricity.

Fɪɢ. 4.—The 95.4% confidence region for the orbit of t1a. Colored squares show orbits in the 95.4% confidence region that we sampled in our orbit-fitting program. Different colors correspond to different levels of confidence: 68.3% (*blue*), 90% (*green*), and 95.4% (*red*). The orbital fits were determined from our *Spitzer* data with $\Delta = 0°.1$. The gray polygon in (*b*) schematically denotes the region of the main asteroid belt. Symbols $\oplus$ in (*b*) denote orbits of all known JFCs with $4° < i < 5°$. While most low-*e* solutions correspond to asteroidal orbits, the tail of the 95.4% confidence region at large *a* and *e* extends to the orbital domain populated by cometary orbits. Two known JFCs, 137P/Shoemaker-Levy 2 ($a = 4.432$ AU, $e = 0.579$, and $i = 4°.6$) and 143P/Kowal-Mrkos ($a = 4.306$ AU, $e = 0.409$, and $i = 4°.6$), that appear closest to the 95.4% confidence region in (*b*) have incompatible $\Omega$ with (*a*).

With $\Delta = 0°.1$, the best-fit orbit matches observed latitudes of t1a in scans C and D to within $30''$ in *b*; we consider this to be a satisfactory precision. The precision is lower with $\Delta = 0°.01$, for which the latitudes agree only to $\approx 80''$. This comparison suggests that the orbits of dust particles do not follow the exact locations of maxima in Figure 3 but rather intersect (on average) the approximate "centers" of each peak that can only be defined from a larger range of latitudes (i.e., from larger $\Delta$).

We used the following method to define a 95.4% confidence region around the best-fit orbit. We normalized $\chi^2$ to $\chi^2_{norm} = \chi^2 N/\chi^2_{min}$, where $\chi^2_{min}$ is the best-fit value of $\chi^2$. The 95.4% confidence region is then a five-dimensional domain in the space of $a, e, i, \omega, \Omega$ in which $\chi^2_{norm} < N + 11.3$ (e.g., Press et al. 1992).

Figure 4 shows that the inclination and nodal longitude of t1a are particularly well defined. The best fits have $i \approx 4°.6$ and $\Omega \approx 85°$. Most orbital solutions also show $e \lesssim 0.3$ and
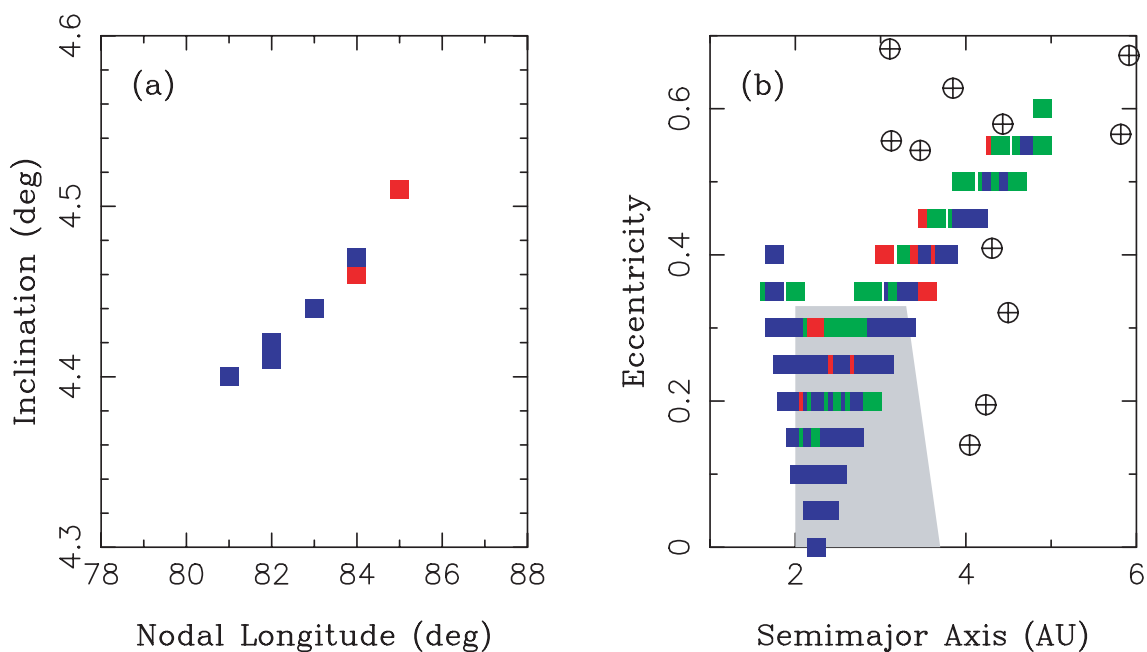


Fɪɢ. 5.—The 95.4% confidence region for the orbit of t1. The color code and symbols are the same as in Fig. 4. The orbital fits were determined from our *Spitzer* data with $\Delta = 0°.6$ for set C and $\Delta = 0°.8$ for set D.
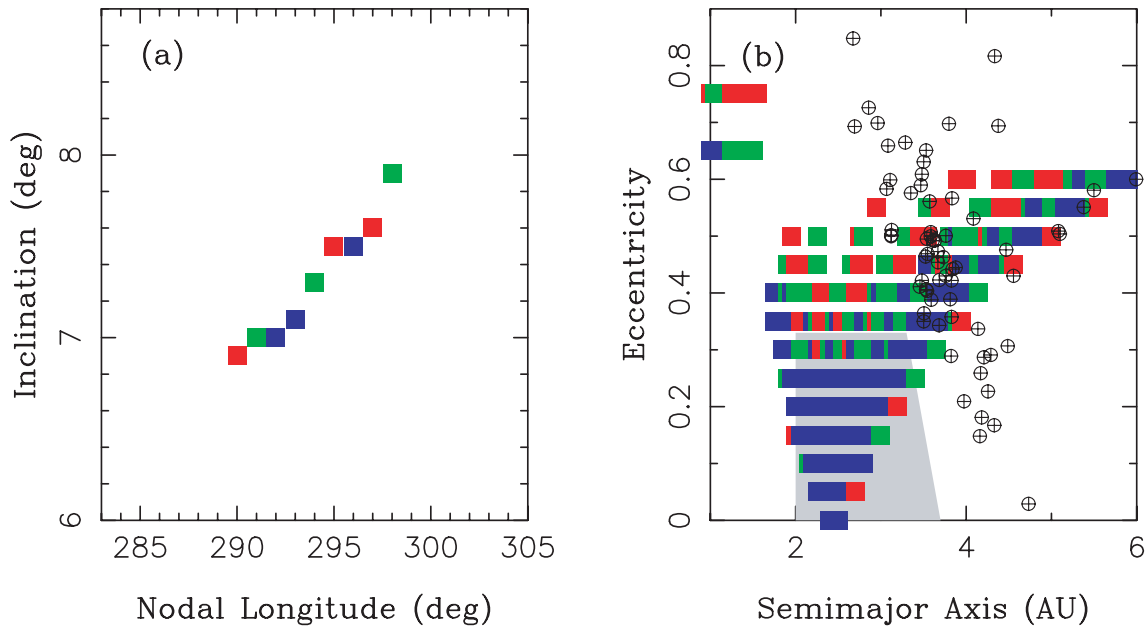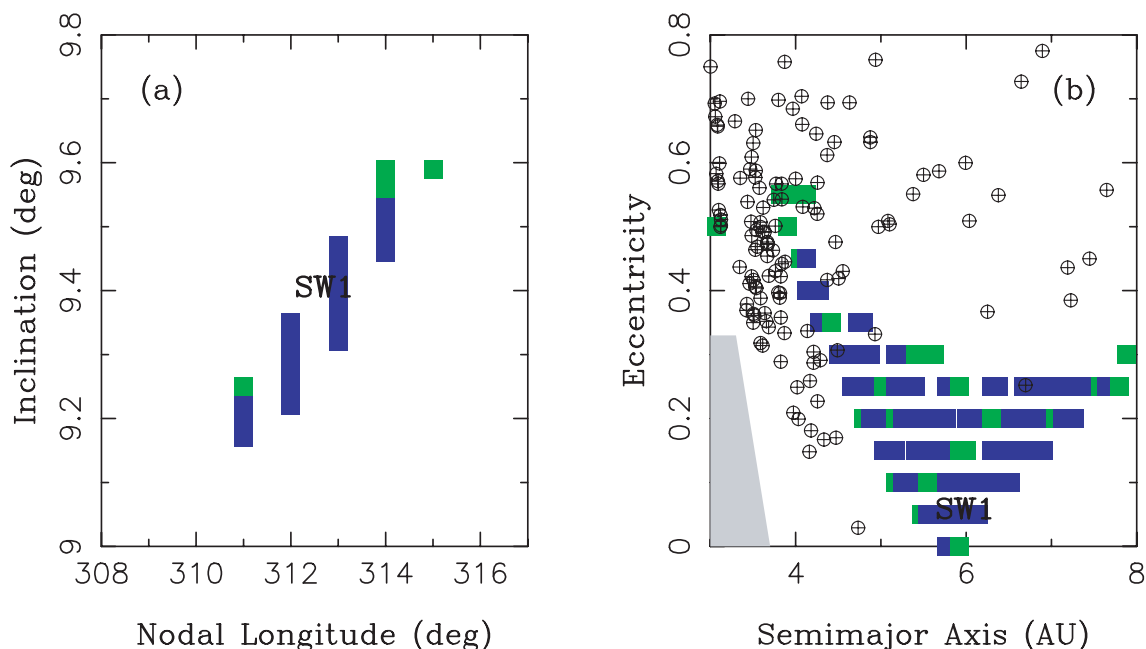
FIG. 6.—The 95.4% confidence region for the orbit of t2. The color code and symbols are the same as in Fig. 4. All known JFCs with $5° < i < 10°$ are plotted in (b). The orbital fits were determined from our *Spitzer* data with $\Delta = 1°$.

1 AU $\lesssim a \lesssim 3$ AU. Perihelion longitudes $\omega$ are not well determined from our observations for the low-$e$ orbits. There are two high-$e$ tails extending to small and large $a$. These tails have $a(1 + e) \approx a_{circ}$ and $a(1 - e) \approx a_{circ}$, respectively, where $a_{circ} = 2.25$ AU. The best-fit values of $\omega$ for these high-$e$ orbital solutions are clustered within $\approx 20°$–$270°$ (for low-$a$ orbits) and to $40°$ (for large-$a$ orbits).

Figure 5 shows our best-fit orbits for t1 determined with larger $\Delta$. These fits show values of $i$ that are about $0°.15$ lower than those obtained for t1a and values of $\Omega$ that are about $2°$ lower. The difference in the best-fit $i$ between t1a and t1 is larger

than the formal errors determined in each case (i.e., 95.4% confidence regions of t1a and t1 in the $i$, $\Omega$ projection do not overlap). This difference probably stems from the fact that we cannot resolve individual orbits in the trail and measure only their collective contribution. Consequently, a larger uncertainty of $i$ and $\Omega$ should be allowed than the formal uncertainty of our orbital fits listed in Table 5.

The 95.4% confidence region in Figure 5a is shaped similarly to that in Figure 4a showing larger $i$ for larger $\Omega$. This correlation between $i$ and $\Omega$ can be readily explained by the way these orbital elements must adjust to match the *Spitzer* observations. The quality



FIG. 7.—The 95.4% confidence region for the orbit of t3. The color code and symbols are the same as in Fig. 4. The orbital fits were determined from our *Spitzer* data with $\Delta = 0°.1$. JFCs with $5° < i < 15°$ are plotted in (b). "SW1" denotes the orbital elements of comet 29P/Schwassmann-Wachmann 1 on 2005 January 1.
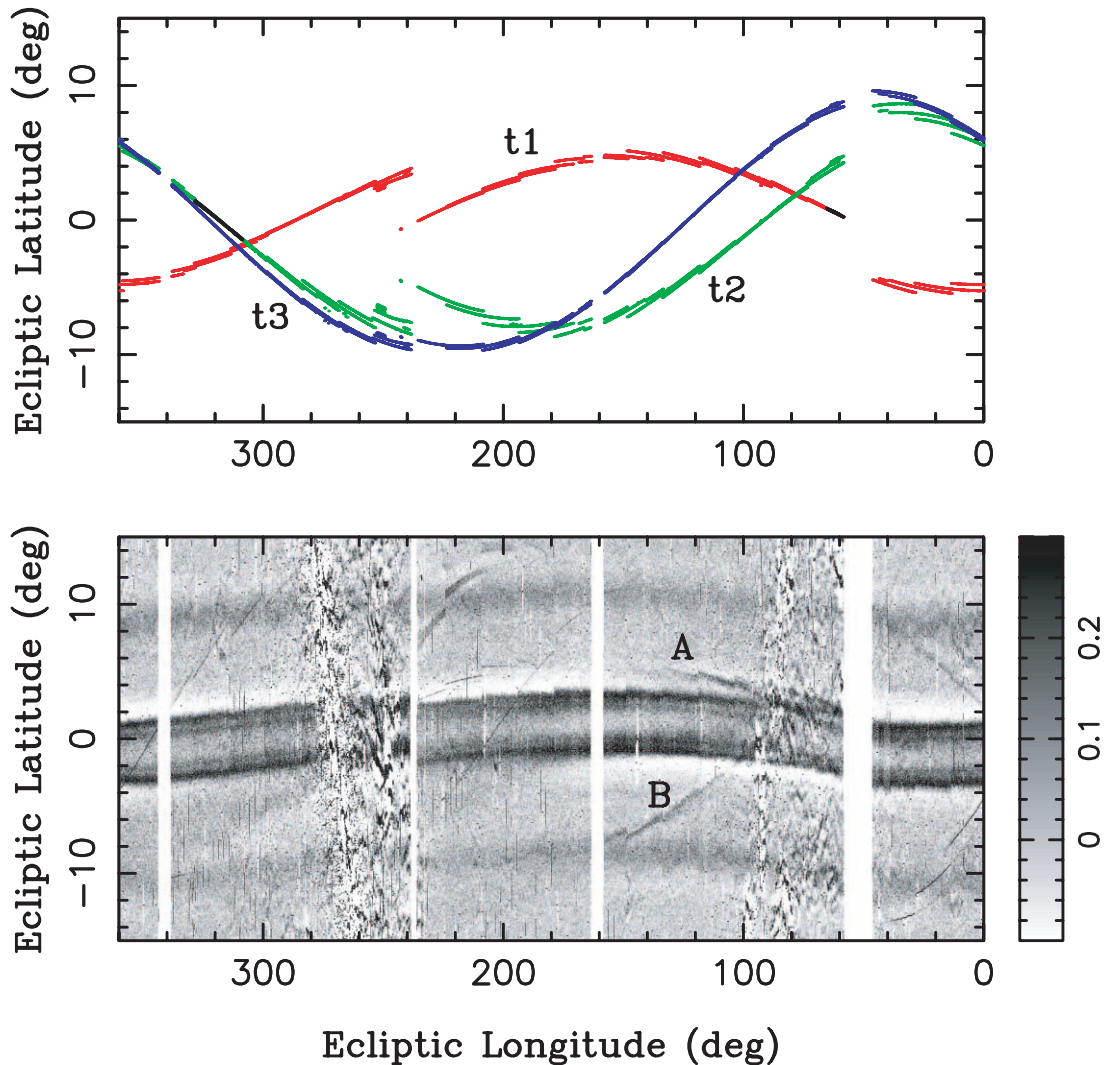
FIG. 8.—*Top:* Expected locations of *Spitzer* trails t1 (*red*), t2 (*green*), and t3 (*blue*) in *IRAS*'s HCONs 1 and 2. For t3 we used the orbit of 29P/Schwassmann-Wachmann 1. For t1 and t2 we used the best-fit orbits from Figs. 5 and 6 with $e = 0$. Projections into HCONs 1 and 2 of the best-fit orbits with larger $e$ show only minor differences compared to those with $e = 0$. *Bottom:* Map constructed from *IRAS*'s 25 $\mu$m HCONs 1 and 2. We have filtered individual scans to remove spatial structures extending $>4°$ and $<0°.1$ in ecliptic latitudes. *IRAS*'s type II trails A and B are denoted. Several comet trails that appear in this plot have been identified by Sykes & Walker (1992) and correspond to comets Tempel 1 and 2, Encke, Kopff, and Gunn. The trail of comet 29P/Schwassmann-Wachmann, which is difficult to see in the bottom plot, has $b \approx -10°$ and $l \approx 200°$ (Sykes & Walker 1992). The close correspondence between the expected locations of *Spitzer*'s trails t1 and t2 in the *IRAS* data and the locations of *IRAS*'s trails A and B, respectively, suggests that t1 is A and t2 is B.

of the best fits for t1's orbit is comparable to those obtained for t1a (i.e., $\approx 25''$ precision in $b$). The value of $\omega$ for the high-$e$ orbits is confined in ways similar to those discussed for t1a above.

Figure 6 shows the best-fit orbits for t2. These fits show larger values of $\chi^2$ than those obtained for t1 (Table 5). The orbital elements of t2 are also not constrained that well. Inclinations are found to be between $7°$ and $8°$, and nodal longitudes range between $290°$ and $298°$. Figure 6b shows that the source of t2 may be asteroidal (if $e < 0.3$) or cometary (if $e > 0.3$). None of the existing comets currently has $i$ and $\Omega$ in (or close to) the 95.4% confidence region shown in Figure 6a. Additional observation data are needed to better determine the orbit of t2.

Figure 7 shows the best-fit orbits for t3. We obtained these orbit solutions by the same method used for trails t1 and t2. The fit constrains the orbital elements in important ways: $9°.2 \lesssim i \lesssim 9°.6$ and $\Omega = 313° \pm 2°$. The predicted orbit has a semimajor axis slightly larger than that of Jupiter and $e \lesssim 0.3$.

For comparison, comet 29P/Schwassmann-Wachmann 1 had the following orbital elements on 2005 January 1: $a = 5.987$ AU, $e = 0.04407$, $i = 9°.391$, $\Omega = 312°.708$, $\omega = 48°.752$, and mean anomaly $M = 11°.911$. The location of this orbit is shown in Figure 7. The similarity of $a$, $e$, $i$, and $\Omega$ between the predicted orbit of t3 and that of comet 29P/Schwassmann-Wachmann 1 reinforces our previous identification of trail t3 with the trail of this comet. It also validates our method of orbit determination for trails from *Spitzer*'s observations.

## 4. RELATION OF t1 AND t2 TO TYPE II TRAILS

Sykes (1988) and Sykes & Walker (1992) identified a number of trails in the *IRAS* data that do not correspond to any known comet. They call them type II, or "orphan," trails. These trails may have detached from their parent comets by Jupiter's orbital perturbations. Alternatively, some type II trails may have been produced by comet or asteroid disruptions. Sykes
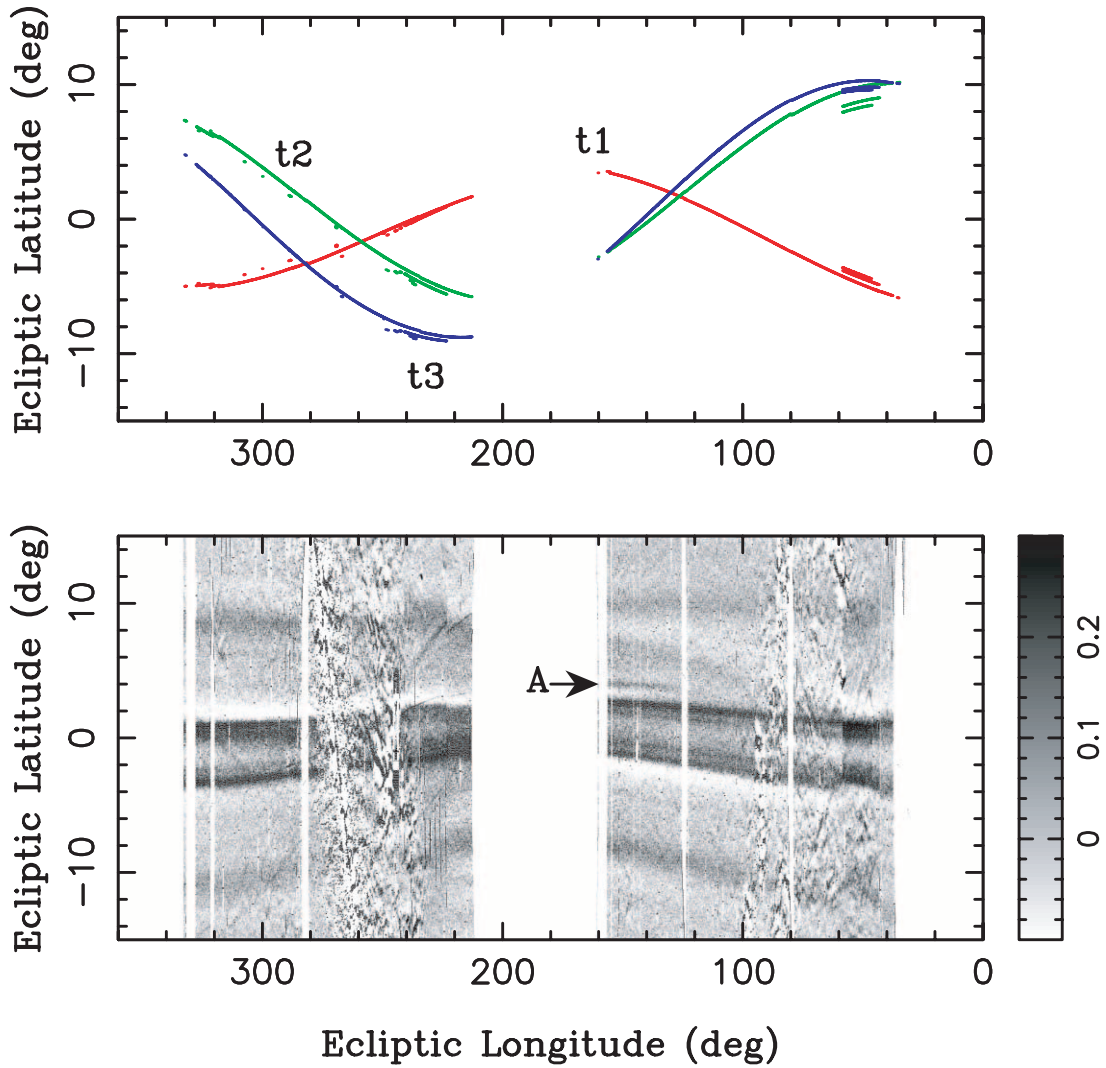
Fig. 9.—*Top:* Expected locations of *Spitzer* trails t1 (*red*), t2 (*green*), and t3 (*blue*) in *IRAS*'s HCON 3. *Bottom:* Map constructed from *IRAS*'s 25 μm HCON 3. See Fig. 8 for further details. The arrow denotes the location of trail A (Sykes 1990).

TABLE 6
*IRAS* Data Used to Determine the Orbit for Trail A

| Scan ID (1) | $t$ (JD) (2) | $l_{IRAS}$ (deg) (3) | $b_{IRAS}$ (deg) (4) | $R_{IRAS}$ (AU) (5) | $l$ (deg) (6) | $b_{max}$ (deg) (7) | $\sigma$ (deg) (8) |
|---|---|---|---|---|---|---|---|
| 029_12........................ | 2,445,374.84861 | 140.25779 | 0.00128 | 0.9866445 | 61.04 | 0.60867 | 0.49848 |
| 122_30........................ | 2,445,421.59349 | 187.08281 | −0.00061 | 0.9980069 | 101.53 | 4.03678 | 0.02533 |
| 146_22........................ | 2,445,433.62227 | 198.94082 | −0.00075 | 1.0015088 | 111.31 | 4.48414 | 0.03221 |
| 183_05........................ | 2,445,451.73489 | 216.64899 | −0.00159 | 1.0064676 | 128.20 | 4.79011 | 0.04814 |
| 574_20........................ | 2,445,647.45744 | 46.20277 | 0.00163 | 0.9906180 | 140.09 | 3.82940 | 0.04080 |
| 587_47........................ | 2,445,654.11148 | 52.89600 | 0.00189 | 0.9890415 | 150.54 | 4.03159 | 0.06496 |

Notes.—We used $\Delta = 0°.7$ here. The columns are: (1) scan identification label; (2) time of the observation; (3)–(5) ecliptic longitude, latitude, and heliocentric distance of *IRAS* at the time shown in col. (2); (6) and (7) *IRAS*-centric ecliptic longitude and latitude of A in each scan; and (8) error of $b_{max}$. Listed values of $\sigma_j$ were determined by the method described in the main text.

TABLE 7
*IRAS* Data Used to Determine the Orbit for Trail B

| Scan ID (1) | $t$ (JD) (2) | $l_{IRAS}$ (deg) (3) | $b_{IRAS}$ (deg) (4) | $R_{IRAS}$ (AU) (5) | $l$ (deg) (6) | $b_{max}$ (deg) (7) | $\sigma$ (deg) (8) |
|---|---|---|---|---|---|---|---|
| 181_07........................ | 2,445,450.80743 | 215.74690 | −0.00158 | 1.0062237 | 126.31 | −5.3089 | 0.3757 |
| 181_11........................ | 2,445,450.87879 | 215.81632 | −0.00158 | 1.0062425 | 126.54 | −5.1049 | 0.0565 |
| 211_18........................ | 2,445,465.98310 | 230.45968 | −0.00169 | 1.0100433 | 143.22 | −6.9045 | 0.0276 |
| 219_02........................ | 2,445,469.70495 | 234.05355 | −0.00189 | 1.0108669 | 135.39 | −5.6094 | 0.0483 |
| 221_06........................ | 2,445,470.77907 | 235.08959 | −0.00195 | 1.0110929 | 137.76 | −5.8484 | 0.0434 |
| 241_01........................ | 2,445,480.73291 | 244.66522 | −0.00214 | 1.0129924 | 152.49 | −8.8289 | 0.0397 |

Notes.—We used $\Delta = 0°.7$. The columns are: (1) scan identification label; (2) time of the observation; (3)–(5) ecliptic longitude, latitude, and heliocentric distance of *IRAS* at the time shown in col. (2); (6) and (7) *IRAS*-centric ecliptic longitude and latitude of B in each scan; and (8) error of $b_{max}$.

(1990, Fig. 2) lists the main type II trails as A, B, C, and D. We use the same notation here.

Figure 8 (*bottom*) shows filtered *IRAS* data corresponding to HCONs 1 and 2.[10] We used the same filter parameters here as for the *Spitzer* data. Trail A extends over about 80° in ecliptic longitude, between $l \approx 60°$ and 140°. Its latitude varies from $b \approx 0°$ for $l = 60°$ to $b \approx 5°$ for $l = 140°$. Trail B extends over at least 60° in $l$, from $\approx 100°$ to $\approx 160°$ (it is not clear whether it continues beyond $l = 100°$, because there is strong Galactic emission at $l < 100°$). Trail B starts at $b \approx 0°$ for $l = 100°$ and goes down to $b \approx -7°$ for $l = 160°$. Trails C and D are more dispersed structures that were not detected in HCONs 1 and 2.

We have taken one of the best orbital fits for our *Spitzer* trails t1 and t2 and projected these orbits onto sky locations where they would be observed by *IRAS*. Figure 8 (*top*) shows this projection. It is apparent from the comparison of the panels in Figure 8 that the predicted locations of trails t1 and t2 in the *IRAS* data correspond well to the locations of *IRAS* trails A and B, respectively. In addition, the brightness and latitudinal spreads of t1 and t2 seen in the *Spitzer* data are comparable to those of *IRAS* trails A and B. We therefore identify t1 with A and t2 with B.

Figure 9 shows the projection of our best-fit orbit into *IRAS*'s HCON 3. Trail B was not found in HCON 3. Trail A appears in HCON 3 as a short line segment about 40° long in $l$, near $l = 140°$ and $b = 4°$. The predicted path of t1 in HCON 3 passes near the observed segment (Fig. 9, *top*) but is slightly more inclined to the ecliptic than the observed trail A and has a bit smaller $b$. In § 5 we compensate for this slight difference by adjusting the best-fit orbits to better match these *IRAS* observations.

## 5. ORBIT FITS FOR t1/a AND t2/b FROM *Spitzer* AND *IRAS* DATA

Having identified trails t1 and t2 with trails A and B in the *IRAS* data, we may now use the location of these trails as determined by *IRAS* observations to improve the orbit determination. Trails A and B are best visible in the 25 $\mu$m *IRAS* filter. We
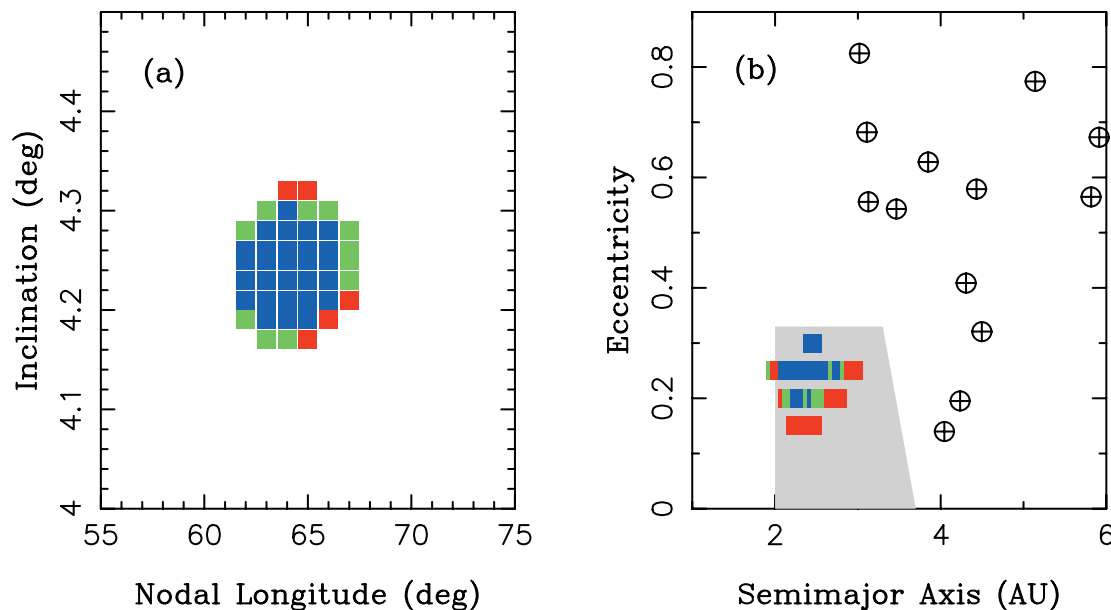
---

[10] Each *IRAS* scan had a width of 0°.5 and was shifted in ecliptic longitude by 0°.25 on the subsequent orbit, allowing a fixed source to be scanned twice in the 103 minute orbital period. This was referred to as an "hours-confirmed observation," or HCON. During the initial portion of its mission, *IRAS* would map out a section of sky (HCON 1) and after about a week remap the same section (HCON 2). During the last 3 months of the mission, a third map (HCON 3) was attempted using a larger range of solar elongations. It covered 72% of the sky before the satellite terminated operations.



Fig. 10.—The 95.4% confidence region for the orbit of t1/A. The color code and symbols are the same as in Fig. 4. JFCs with $4° < i < 5°$ are plotted in (*b*). The orbital elements of t1/A have been determined by combining *Spitzer* and *IRAS* observations of this trail.
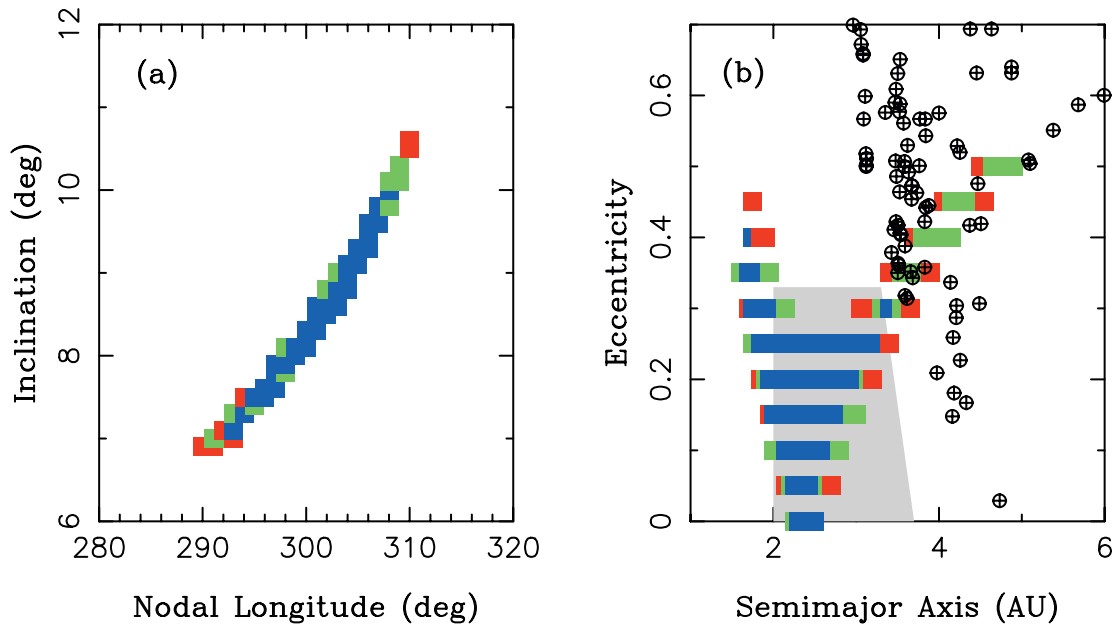
Fig. 11.—The 95.4% confidence region for the orbit of t2/B. The color code and symbols are the same as in Fig. 4. JFCs with $6° < i < 12°$ are plotted in (b). The orbital elements have been determined by combining *Spitzer* and *IRAS* observations of this trail.

selected several 25 $\mu$m *IRAS* scans in which these trails can be readily identified. Information about these scans is listed in Tables 6 and 7. To identify the exact latitudinal locations of trails A and B in each scan, we used the polynomial fit method described in § 3. The *IRAS* data are significantly noisier than the *Spitzer* data. Therefore, the formal errors of $b_{max}$ determined by the polynomial fit are relatively large.

We first attempted to fit for the orbits of trails A and B using the *IRAS* data alone. These orbital fits are listed in Table 5. The quality of the orbital fits is significantly lower than those obtained for t1 and t2 from *Spitzer*; the best-fit orbits match the *IRAS* observations of trails A and B to within 9′ and 30′, respectively (compared to about an order of magnitude better precision with *Spitzer*).

For trail A, the best-fit orbits have $60° \lesssim \Omega \lesssim 70°$, $4°2 \lesssim i \lesssim 4°8$, $e \lesssim 0.3$, and $2$ AU $\lesssim a \lesssim 4$ AU. This range of orbital elements is comparable to those obtained for t1 from *Spitzer*. Interestingly, most orbits of trail A as determined from the *IRAS* data have low eccentricities and $a$ in the range of the main asteroid belt.

Nodal longitude $\Omega$ determined for trail A from *IRAS* is smaller by $10°$–$20°$ than values of $\Omega$ determined for t1 from *Spitzer*. It is unlikely that this difference was produced by the secular precession of $\Omega$ between 1983.5 (epoch of *IRAS* observations) and 2005 (epoch of *Spitzer* observations), because planetary perturbations cause $\dot{\Omega} < 0$ and small $|\dot{\Omega}|$, while large and positive $\dot{\Omega}$ would be needed to shift $\Omega$ by $10°$–$20°$ in 21.5 yr.

Assuming that the orbit of t1/A has not changed in the interim period, we searched for the best-fit orbits of t1/A from both *Spitzer* and *IRAS* observations. These orbits match $b_{max}$ in the *Spitzer* data to about 2′ (compared to 0′.4 when only *Spitzer* data were used) and the $b_{max}$ in the *IRAS* data to ≈10′. The combined fit requires that $2$ AU $< a < 3$ AU and $0.15 < e < 0.3$ (Fig. 10). This range of $a$ and $e$, and small values of $i$ that we consistently obtain for t1 from all data sets, suggests that the source of t1/A may be asteroidal. The combined fit requires that $4°15 < i < 4°35$, $61° < \Omega < 67°$, and $140° < \omega < 220°$.

We performed a number of tests to see how the orbital fits determined from the combined *Spitzer* and *IRAS* data depend on the selection of scans used in the orbit-fitting program. For example, we combined the *Spitzer* data with *IRAS*'s HCONs 1 and 2 only and fitted for orbits from 12 data points (eight *Spitzer* data points from Table 2 and four *IRAS* data points corresponding to HCONs 1 and 2; Table 6, *first four rows*). The best-fit orbits determined in this test have a slightly larger range of $i$ and $\Omega$ than that in Figure 10. Like in Figure 10, however, most of the best-fit orbits are located in the main asteroid belt. This result shows that our conclusion about the asteroidal origin of trail t1/A does not rely on the input from *IRAS*'s HCON 3.

The orbital fits for trail B from the *IRAS* data show a large spread in $a$ and $e$. This is due to the fact that trail B has been observed in HCONs 1 and 2 only where the solar elongation of the telescope's pointing direction did not vary much. It is therefore difficult to determine the orbit from *IRAS* data only. When *Spitzer* and *IRAS* data are used together, however, we find that most best-fit orbits for t2/B are asteroidal (Fig. 11). Despite this, there exists a tail of solutions with large $a$ and $e$ that correspond to cometary orbits. Additional data will be needed to better constrain the orbit of t2/B.

## 6. DISCUSSION

Our orbital fits suggest that the source of trail t1 may be asteroidal. This conclusion relies on the combined fits in which *Spitzer* and *IRAS* observations were used together. While useful, it is not ideal to combine these data sets, because (1) *IRAS* data are relatively noisy, making it more difficult to determine the exact latitudinal locations of trails, and (2) we must assume that orbits did not change much in the period between *IRAS* and *Spitzer* observations. Assumption (2) is likely to be correct if the source has a stable orbit in the main asteroid belt. If, however, the orbit was Jupiter-crossing (e.g., a JFC's orbit), encounters with Jupiter may have modified it, and assumption (2) may be incorrect.

A recent collisional breakup of a main-belt asteroid would not only produce a strong dust trail, but the large fragments released
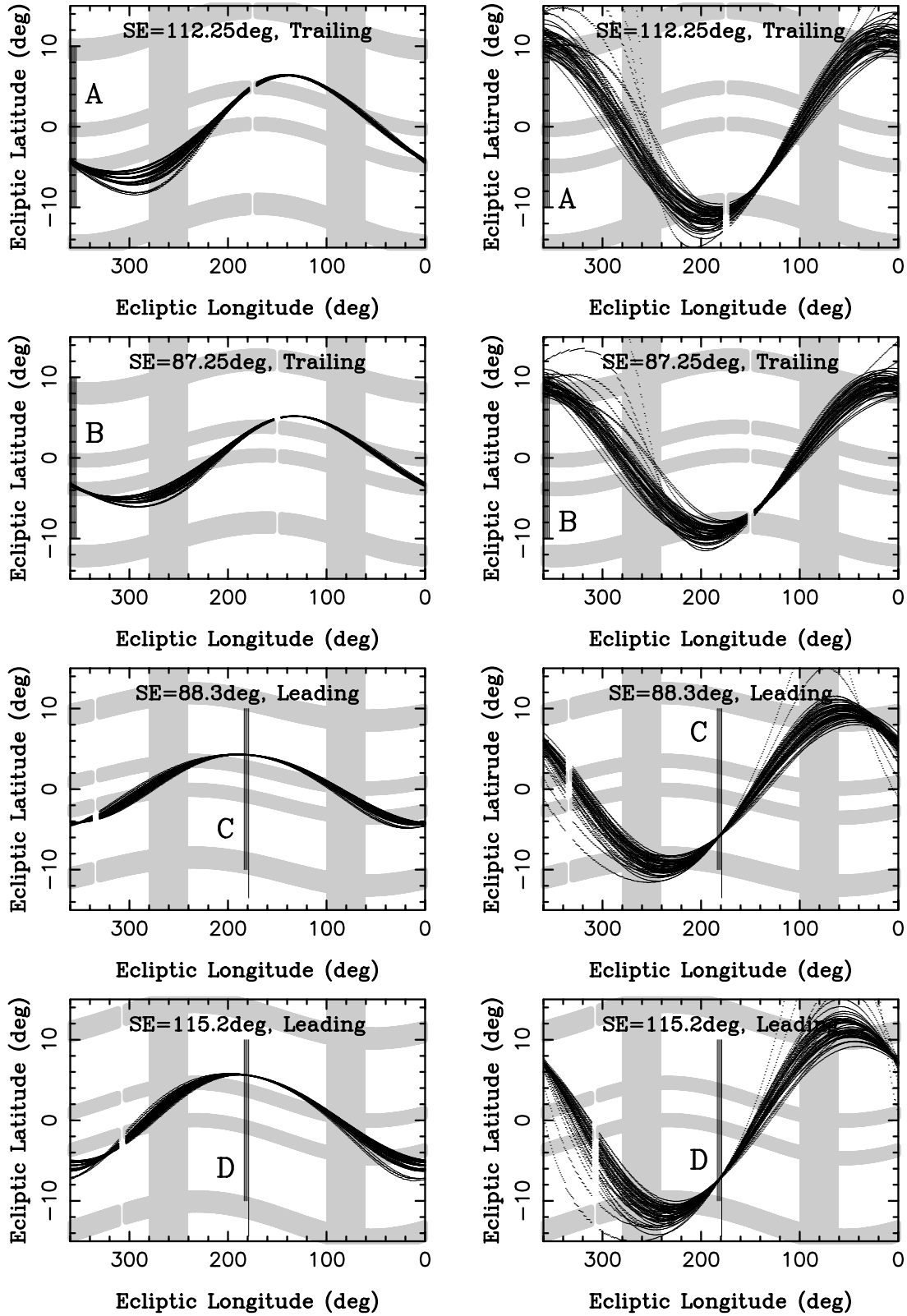
Fig. 12.—Expected locations of trails t1/A (*left panels*) and t2/B (*right panels*) as seen by *Spitzer* during Cycle 1 from 2004 June 1 to 2005 May 31. To make these plots, we assumed four different observing solar elongations, $112°25$, $87°25$, $88°3$, and $115°2$, corresponding to our noodles A, B, C, and D, respectively (*top to bottom*). The individual four scans in each set are shown by vertical line segments separated by $1°5$ in ecliptic longitude. The sinusoidal lines show projections of orbits for trails t1/A and t2/B that were determined from our *Spitzer* Cycle 1 and the *IRAS* data. Gray areas show locations of the inner and outer asteroid dust bands and the Galactic emission.

during the breakup could also potentially create an observable asteroid family. We searched for asteroid families that would have orbital elements near those predicted for t1 and t2. We used the hierarchical clustering method (Zappalà et al. 1990) with a generalized metric in the five-dimensional space of osculating orbital elements: $a$, $e$, $i$, $\omega$, and $\Omega$ (see Nesvorný et al. 2006a; Nesvorný & Vokrouhlický 2006). We found no obvious clusters that could be linked with t1 or t2. This result probably implies that the disrupted body was small, perhaps only several kilometers across, such that the largest fragments produced by the breakup have sizes below the current detection limit. According to Bottke et al. (2005), a 1 km diameter asteroid disrupts in the main belt every $\sim$100 yr and a 10 km diameter asteroid every $\sim$100 kyr.

If the ejection speeds of fragments, $\delta V$, from these disruptions were of the order of 10 m s$^{-1}$, we estimate that the fragments were spread in semimajor axis by $\delta a = 4a\delta V/V \sim 5 \times 10^{-3}$ AU, where $V \approx 20$ km s$^{-1}$ is the orbital speed for $a = 2.3$ AU. Having different semimajor axes, the fragments then started to differentially spread in mean anomaly $M$, $\omega$, and $\Omega$.

Particles in trails t1 and t2 must have narrow spreads in $\Omega$ at the current epoch (we would not otherwise obtain good orbital fits). This sets a firm upper limit on the age of these trails. Using the results of Sykes & Greenberg (1986), we estimate that trails t1 and t2 cannot be older than $\sim$100 kyr. A detailed model of the differential precession of nodes could be used to better constrain the age of trails t1 and t2. This model will have to include effects of radiation forces such as Poynting-Robertson drag and account for collisional disruptions of migrating small particles. Such a model could also be useful to explain the double-peaked structure of trail t1 (Fig. 3).

The lengths of observed trails A and B in the *IRAS* data may provide additional constraints on the age. There are two possibilities: (1) due to favorable observing conditions, *IRAS* detected only parts of trails A and B, which are actually spread over 360° in $M$ (i.e., trails are tubes); or (2) the lengths of the observed arcs directly correspond to the spread of particles in $M$ (i.e., trails are arcs). As for (1), we estimate that the variation of 24 $\mu$m brightness of trails t1/A and t2/B from perihelion to aphelion of their asteroidal orbits should be a factor of a few. It is not obvious whether this variation is large enough to favor (1).

Unfortunately, it is also difficult to determine whether *Spitzer* and *IRAS* could have observed the same arc of trails t1 and t2.

This is due to the fact that the uncertainty in the semimajor axis of trails is large, so $M$ cannot be reliably tracked over the time period that separates the *IRAS* and *Spitzer* observations (about 21.5 yr). Conversely, the nondetection of trails t1 and t2 in noodles A and B could provide a better constraint on the extension of trails because of the sensitivity of *Spitzer* observations and because all our observations were taken within a period of only 2 months (so that particles did not move much along their orbits).

To help address this issue we determined the expected ecliptic coordinates of trails t1/A and t2/B that correspond to the observing geometry of *Spitzer* during Cycle 1. Figure 12 shows that scans A and B were not sufficiently extended above the ecliptic plane to cross over the expected location of trail t2/B ($b \approx 10°{-}12°$). It is therefore not surprising that this trail was not detected in our sets A and B. Conversely, the expected location of trail t1/A in scans A and B is $b \approx -4°$, well within the scanned interval of ecliptic latitudes. It is unfortunate, however, that the strong south component of the inner dust band is also located at $b \approx -4°$. A weaker signal of trail t1/A may then be hidden and easily overlooked at this latitude. The nondetection of trails in scans A and B cannot, therefore, be used to favor (2). The question of whether trails t1/A and t2/B are arcs or tubes remains open.

The cometary origin of trail t2/B cannot be strictly excluded with the present data because our orbital fits allow for some orbit solutions with comet-like large $e$. Additional observations are needed to resolve this issue. Ideally, we would plan the observations to obtain scans with *Spitzer* at several different ecliptic longitudes, at least two different solar elongations, and across the latitude values predicted for the orbits determined here. Such observations would be extremely useful to determine (1) the orbits of t1/A and t2/B precisely and (2) whether the trails are arcs or tubes. The results would have major implications for our understanding of the age of the observed trails and the overall contribution of small asteroid breakups to the zodiacal cloud.

## REFERENCES

Bottke, W. F., Durda, D. D., Nesvorný, D., Jedicke, R., Morbidelli, A., Vokrouhlický, D., & Levison, H. F. 2005, Icarus, 179, 63
Dermott, S. F., Nicholson, P. D., Burns, J. A., & Houck, J. R. 1984, Nature, 312, 505
Greaves, J. S., Wyatt, M. C., Holland, W. S., & Dent, W. R. F. 2004, MNRAS, 351, L54
Greaves, J. S., et al. 2005, ApJ, 619, L187
Grogan, K., Dermott, S. F., & Durda, D. D. 2001, Icarus, 152, 251
Jopek, T. J., Valsecchi, G. B., & Froeschlé, C. 2002, in Asteroids III, ed. W. F. Bottke et al. (Tucson: Univ. Arizona Press), 645
Low, F. J., et al. 1984, ApJ, 278, L19
Nesvorný, D., Bottke, W. F., Levison, H., & Dones, L. 2002, Nature, 417, 720
———. 2003, ApJ, 591, 486
Nesvorný, D., & Vokrouhlický, D. 2006, AJ, submitted
Nesvorný, D., Vokrouhlický, D., & Bottke, W. F. 2006a, Science, in press

Nesvorný, D., Vokrouhlický, D., Bottke, W. F., & Sykes, M. 2006b, Icarus, 181, 107
Press, W. H., Teukolsky, S. A., Vetterling, W. T., & Flannery, B. P. 1992, Numerical Recipes in C (2nd ed.; Cambridge: Cambridge Univ. Press)
Reach, W. T., Franz, B. A., & Weiland, J. L. 1997, Icarus, 127, 461
Reach, W. T., Sykes, M. V., Lien, D., & Davies, J. K. 2000, Icarus, 148, 80
Stansberry, J. A., et al. 2004, ApJS, 154, 463
Sykes, M. V. 1986, Ph.D. thesis, Univ. Arizona
———. 1988, ApJ, 334, L55
———. 1990, Icarus, 85, 267
Sykes, M. V., & Greenberg, R. 1986, Icarus, 65, 51
Sykes, M. V., & Walker, R. G. 1992, Icarus, 95, 180
Zappalà, V., Cellino, A., Farinella, P., & Knežević, Z. 1990, AJ, 100, 2030